

A Giant Planet beyond the Snow Line in Microlensing Event OGLE-2011-BLG-0251

N. Kains^{1,*}, R. A. Street², J.-Y. Choi³, C. Han^{3,**}, A. Udalski⁴, L. A. Almeida⁵, F. Jablonski⁵,
P.J. Tristram⁶, U.G. Jørgensen^{7,8},

and

M. K. Szymański⁴, M. Kubiak⁴, G. Pietrzyński^{4,69}, I. Soszyński⁴, R. Poleski⁴, S. Kozłowski⁴, P.
Pietrukowicz⁴, K. Ulaczyk⁴, Ł. Wyrzykowski^{34,4}, J. Skowron^{24,4}

(The OGLE collaboration)

and

K.A. Alsubai⁹, V. Bozza^{10,11}, P. Browne¹², M.J. Burgdorf^{13,14}, S. Calchi Novati^{10,15}, P. Dodds¹², M.
Dominik^{12,***}, S. Dreizler¹⁶, X.-S. Fang¹⁸, F. Grundahl¹⁹, C.-H. Gu¹⁸, S. Hardis⁷, K. Harpsøe^{7,8}, F.V.
Hessman¹⁶, T.C. Hinse^{17,7,20}, A. Hornstrup²², M. Hundertmark^{12,16}, J. Jessen-Hansen¹⁹, E. Kerins²², C.
Liebig¹², M. Lund¹⁹, M. Lundkvist¹⁹, L. Mancini²³, M. Mathiasen⁷, M.T. Penny^{22,24}, S. Rahvar^{25,26}, D.
Ricci²⁷, K.C. Sahu²⁸, G. Scarpetta^{10,29}, J. Skottfelt⁷, C. Snodgrass³¹, J. Southworth³², J. Surdej²⁷, J.
Tregloan-Reed³², J. Wambsganss³³, O. Wertz²⁷

(The MiNDSTEp consortium)

and

D. Bajek¹², D.M. Bramich¹, K. Horne¹², S. Ipatov³⁵, I.A. Steele³⁶, Y. Tsapras^{2,37}

(The RoboNet collaboration)

and

F. Abe⁵⁹, D.P. Bennett⁶⁰, I.A. Bond⁶¹, C.S. Botzler⁶², P. Chote⁶, M. Freeman⁶², A. Fukui⁶³,
K. Furusawa⁵⁹, Y. Itow⁵⁹, C.H. Ling⁶¹, K. Masuda⁵⁹, Y. Matsubara⁵⁹, N. Miyake⁵⁹, Y. Muraki⁶⁵,
K. Ohnishi⁶⁶, N. Rattenbury⁶², T. Saito⁶⁷, D.J. Sullivan⁶, T. Sumi⁶⁸, D. Suzuki⁶⁸, K. Suzuki⁵⁹,
W.L. Sweatman⁶¹, S. Takino⁵⁹, K. Wada⁶⁸, P.C.M. Yock⁶²

(The MOA collaboration)

and

W. Allen³⁸, V. Batista²⁴, S.-J. Chung¹⁷, G. Christie³⁹, D.L. DePoy⁴⁰, J. Drummond⁴¹, B.S. Gaudi²⁴, A.
Gould²⁴, C. Henderson²⁴, Y.-K. Jung³, J.-R. Koo¹⁷, C.-U. Lee¹⁷, J. McCormick⁴², D. McGregor²⁴,
J.A. Muñoz⁴⁵, T. Natusch^{39,43}, H. Ngan³⁹, H. Park³, R.W. Pogge²⁴, I.-G. Shin³, J. Yee²⁴

(The μ FUN collaboration)

and

M.D. Albrow⁴⁷, E. Bachelet^{52,53}, J.-P. Beaulieu⁴⁶, S. Brillant³⁰, J.A.R. Caldwell⁴⁸, A. Cassan⁴⁶,
A. Cole⁵⁰, E. Corrales⁴⁶, Ch. Coutures⁴⁶, S. Dieters⁵², D. Dominis Prester⁵⁴, J. Donatowicz⁵⁵,
P. Fouqué^{52,53}, J. Greenhill⁵⁰, S.R. Kane⁵⁶, D. Kubas^{30,46}, J.-B. Marquette⁴⁶, R. Martin⁵⁷,
P. Meintjes⁴⁹, J. Menzies⁵⁸, K.R. Pollard⁴⁷, A. Williams³³, D. Wouters⁴⁶, and M. Zub³³

(The PLANET collaboration)

(Affiliations can be found after the references)

Received ... ; accepted ...

Abstract

Aims. We present the analysis of the gravitational microlensing event OGLE-2011-BLG-0251. This anomalous event was observed by several survey and follow-up collaborations conducting microlensing observations towards the Galactic Bulge.

Methods. Based on detailed modelling of the observed light curve, we find that the lens is composed of two masses with a mass ratio $q = 1.9 \times 10^{-3}$. Thanks to our detection of higher-order effects on the light curve due to the Earth's orbital motion and the finite size of source, we are able to measure the mass and distance to the lens unambiguously.

Results. We find that the lens is made up of a planet of mass $0.53 \pm 0.21 M_J$ orbiting an M dwarf host star with a mass of $0.26 \pm 0.11 M_\odot$. The planetary system is located at a distance of 2.57 ± 0.61 kpc towards the Galactic Centre. The projected separation of the planet from its host star is $d = 1.408 \pm 0.019$, in units of the Einstein radius, which corresponds to 2.72 ± 0.75 AU in physical units. We also identified a competitive model with similar planet and host star masses, but with a smaller orbital radius of 1.50 ± 0.50 AU. The planet is therefore located beyond the snow line of its host star, which we estimate to be around $\sim 1 - 1.5$ AU.

Key words. gravitational lensing – extrasolar planets – modelling

1. Introduction

Gravitational microlensing is one of the methods that allows us to probe the populations of extrasolar planets in the Milky Way, and has now led to the discoveries of 16 planets¹, several of which could not have been detected with other techniques (e.g. Beaulieu et al. 2006, Gaudi et al. 2008, Muraki et al. 2011). In particular, microlensing events can reveal cool, low-mass planets that are difficult to detect with other methods. Although this method presents several observational and technical challenges, it has recently led to several significant scientific results. Sumi et al. (2011) analysed short time-scale microlensing events and concluded that these events were produced by a population of Jupiter-mass free-floating planets, and were able to estimate the number of such objects in the Milky Way. Cassan et al. (2012) used 6 years of observational data from the PLANET collaboration to build on the work of Gould et al. (2010) and Sumi et al. (2011), and derived a cool planet mass function, suggesting that, on average, the number of planets per star is expected to be more than 1.

Modelling gravitational microlensing events has been and remains a significant challenge, due to a complex parameter space and computationally demanding calculations. Recent developments in modelling methods (e.g. Cassan 2008; Kains et al. 2009, 2012; Bennett 2010; Ryu et al. 2010; Bozza et al. 2012), however, have allowed microlensing observing campaigns to optimise their strategies and scientific output, thanks to real-time modelling providing prompt feedback to observers as to the possible nature of ongoing events.

In this paper we present an analysis of microlensing event OGLE-2011-BLG-0251, an anomalous event discovered during the 2011 season by the OGLE collaboration and observed intensively by follow-up teams. In Sec. 2, we briefly summarise the basics of relevant microlensing formalism, while we discuss our data and reduction in Sec. 3. Our modelling approach and results are outlined in Sec. 4; we translate this into physical parameters of the lens system in Sec. 5 and discuss the properties of the planetary system we infer.

2. Microlensing formalism

Microlensing can be observed when a source becomes sufficiently aligned with a lens along the line of sight that the deflection of the source light by the lens is significant. A characteristic separation at which this occurs is the Einstein ring radius. When a single point source approaches a single point lens of mass M with a projected source-lens separation u , the source brightness is magnified following a symmetric “point source-point lens” (PSPL) pattern which can be parameterised with an impact parameter u_0 and a timescale t_E , both expressed in units of the angular Einstein radius (Einstein 1936),

$$\theta_E = \sqrt{\frac{4GM}{c^2} \left(\frac{D_S - D_L}{D_S D_L} \right)}, \quad (1)$$

where G is the gravitational constant, c is the speed of light, and D_S and D_L are the distances to the source and the lens, respectively, from the observer. The timescale is then $t_E = \theta_E/\mu$, where μ is the lens-source relative proper motion. Therefore the observable t_E is a degenerate function of M, D_L and the source’s transverse velocity v_\perp , assuming that D_S is known. However, measuring certain second-order effects in microlensing light curves such as the parallax due to the Earth’s orbit allows us to break this degeneracy and therefore measure the properties of the lensing system directly.

When the lens is made up of two components, the magnification pattern can follow many different morphologies, because of singularities in the lens equation. These lead to source positions, along closed *caustic* curves, where the lensing magnification is formally infinite for point sources, although the finite size of sources means that, in practice, the magnification gradient is large rather than infinite. A point-source binary-lens (PSBL) light curve is often described by 6 parameters: the time at which the source passes closest to the center of mass of the binary lens, t_0 , the Einstein radius crossing time, t_E , the minimum impact parameter u_0 , which are also used to describe PSPL light curves, as well as the source’s trajectory angle α with respect to the lens components, the separation between the two mass components, d , and their mass ratio q . Finite source size effects can be parameterised in a number of ways, usually by defining the angular size of the source ρ_* in units of θ_E :

$$\rho_* = \frac{\theta_*}{\theta_E}, \quad (2)$$

where θ_* is the angular size of the source in standard units.

3. Observational data

The microlensing event OGLE-2011-BLG-0251 was discovered by the OGLE (Optical Gravitational Lens Experiment) collaboration’s Early Warning System (Udalski 2003) as part of the release of the first 431 microlensing alerts following the OGLE-IV upgrade. The source of the event has equatorial coordinates $\alpha = 17^h 38^m 14.18^s$ and $\delta = -27^\circ 08' 10.1''$ (J2000.0), or Galactic coordinates of $(l, b) = (0.670^\circ, 2.334^\circ)$. Anomalous behaviour was first detected and alerted on August 9, 2011 (HJD ~ 2455782.5) thanks to real-time modelling efforts by various follow-up teams that were observing the event, but by that time a significant part of the anomaly had already passed, with sub-optimal coverage due to unfavourable weather conditions. The anomaly appears as a two-day feature spanning HJD = 2455779.5 to 2455781.5, just before the time of closest approach t_0 . Despite difficult weather and moonlight conditions, the anomaly was securely covered by data from five follow-up telescopes in Brazil (μ FUN Pico dos Dias), Chile (MiNDSTeP Danish 1.54m) New Zealand (μ FUN Vintage Lane, and MOA Mt. John B&C), and the Canary Islands (RoboNet Liverpool Telescope).

The descending part of the light curve also suffered from the bright Moon, with the source ~ 5 degrees from the Moon at $\sim 85\%$ of full illumination, leading to high background counts in images and more scatter in the reduced data. We opted not to include data from Mt. Canopus 1m

* corresponding author; nkains@eso.org

** corresponding author; cheongho@astroph.chungbuk.ac.kr

*** Royal Society University Research Fellow

¹ <http://exoplanet.eu>

telescope in the modelling because of technical issues at the telescope affecting the reliability of the images, and also excluded the I -band data from CTIO because they also suffer from large scatter, probably due to the proximity of the bright full Moon to the source.

The data set amounts to 3738 images from 13 sites, from the OGLE survey team, the MiNDSTeP consortium, the RoboNet team, as well as the μ FUN, PLANET and MOA collaborations in the I , V and R bands, as well as some unfiltered data; data sets are summarised in Table 1 and the light curve is shown in Fig. 1. We reduced all data using the difference imaging pipeline DanDIA (Bramich 2008; Bramich et al. 2013), except for the OGLE data, which was reduced by the OGLE team with their optimised offline pipeline.

For each data set, we applied an error bar rescaling factors a and b to normalise error bars with respect to our best-fit model (see Sec. 4), using the simple scaling relation $\sigma'_i = a\sqrt{\sigma_i^2 + b^2}$ where σ'_i is the rescaled error bar of the i^{th} data point and σ_i is the original error bar. The error bar rescaling factors for each data set is given in Table 1. We did not exclude outliers from our data sets, unless we had reasons to believe that an outlier had its origin in a bad observation, or in issues with the data reduction pipeline.

4. Modelling

We modelled the light curve of the event using a Markov Chain Monte Carlo (MCMC) algorithm with adaptive step size. We first used the “standard” PSBL parameterisation in our modelling, whereby a binary-lens light curve can be described by 6 parameters: those given in Sec. 2, ignoring the second-order ρ_* parameter described in that section. For all models and configurations we searched the parameter space for solutions with both a positive and a negative impact parameter u_0 .

We started without including second-order effects of the source having a finite size or parallax due to the orbital motion of Earth around the Sun, and then added these separately in subsequent modelling runs by fitting the source size parameter ρ_* , as defined in Sec. 2, and the parallax parameters described below. Both effects led to a large decrease in the χ^2 statistic of the model (> 1000), which could not be explained only by the extra number of parameters.

For the finite-source effect, we additionally considered the limb-darkening variation of the source star surface brightness by modelling the surface-brightness profile as

$$I_{\psi,\lambda} = I_{0,\lambda}[1 - c_l(1 - \cos\psi)], \quad (3)$$

where $I_{0,\psi}$ is the brightness at the centre of the source, and ψ is the angle between a normal to the surface and the line of sight. We adopt the limb-darkening coefficients based on the source type determined from the dereddened colour and brightness (see Sec. 5.1). The values of the adopted coefficients are $c_V = 0.073$, $c_I = 0.624$, $c_R = 0.542$, based on the catalogue of Claret (2000).

Finally, in a third round of modelling, we included both the effects of parallax and finite source size (“ESBL + parallax”). Including these effects together led to a significant improvement of the fit, with $\Delta\chi^2 > 500$ compared to the fits in which those effects were added separately. Computing the f -statistic (see e.g. Lupton 1993) for this difference tells us that the probability of this difference occurring solely

due to the number of degrees of freedom decreasing by 1 or 2 is highly unlikely. Our best-fit ESBL + parallax model is shown in Fig. 1.

To model the effect of parallax, we used the geocentric formalism (Dominik 1998; An et al. 2002; Gould 2004), which has the advantage of allowing us to obtain a good estimate of t_0 , t_E and u_0 from a fit that does not include parallax. This formalism adds a further 2 parallax parameters, $\pi_{E,E}$ and $\pi_{E,N}$, the components of the lens parallax vector $\boldsymbol{\pi}_E$ projected on the sky along the east and north equatorial coordinates, respectively. The amplitude of $\boldsymbol{\pi}_E$ is then

$$\pi_E = \sqrt{\pi_{E,E}^2 + \pi_{E,N}^2}. \quad (4)$$

Measuring π_E in addition to the source size allows us to break the degeneracy between the mass, distance and transverse velocity of the lens system that is seen in Eq. (1). This is because π_E also relates to the lens and source parallaxes π_L and π_S as

$$\pi_E = \frac{\pi_L - \pi_S}{\theta_E} = \frac{D_L^{-1} - D_S^{-1}}{\theta_E}. \quad (5)$$

Using this in Eq. (1) allows us to solve for the mass of the lens.

As an additional second-order effect, we also consider the orbital motion of the binary lens. Under the approximation that the change rates of the binary separation and the rotation of the binary axis are uniform during the event, the orbital effect is taken into consideration with 2 additional parameters of \dot{d} and $\dot{\alpha}$, which represent the rate of change of the binary separation and the source trajectory angle with respect to the binary axis, respectively. It is found that the improvement of fits by the orbital effect is negligible and thus our best-fit model is based on a static binary lens.

Below we outline our modelling efforts that resulted in fits that were not competitive with our best-fit ESBL + parallax models, and which we therefore excluded in our light curve interpretation.

4.1. Excluded models

4.1.1. Xallarap

We attempted to model the effects of so-called xallarap, orbital motion of the source if it has companion (Griest & Hu 1992). Modelling this requires five additional parameters: the components of the xallarap vector, $\xi_{E,N}$ and $\xi_{E,E}$, the orbital period P , inclination i and the phase angle ψ of the source orbital motion. By definition, the magnitude of the xallarap vector is the semi-major axis of the source’s orbital motion with respect to the centre of mass, a_S , normalised by the projected Einstein radius onto the source plane, $\hat{r}_E = D_S\theta_E$, i.e.

$$\xi_E = a_S/\hat{r}_E. \quad (6)$$

The value of a_S is then related to the semi-major axis of the binary by

$$a_S = \frac{a M_2}{M_1 + M_2}, \quad (7)$$

where M_1 and M_2 are the masses of the source components.

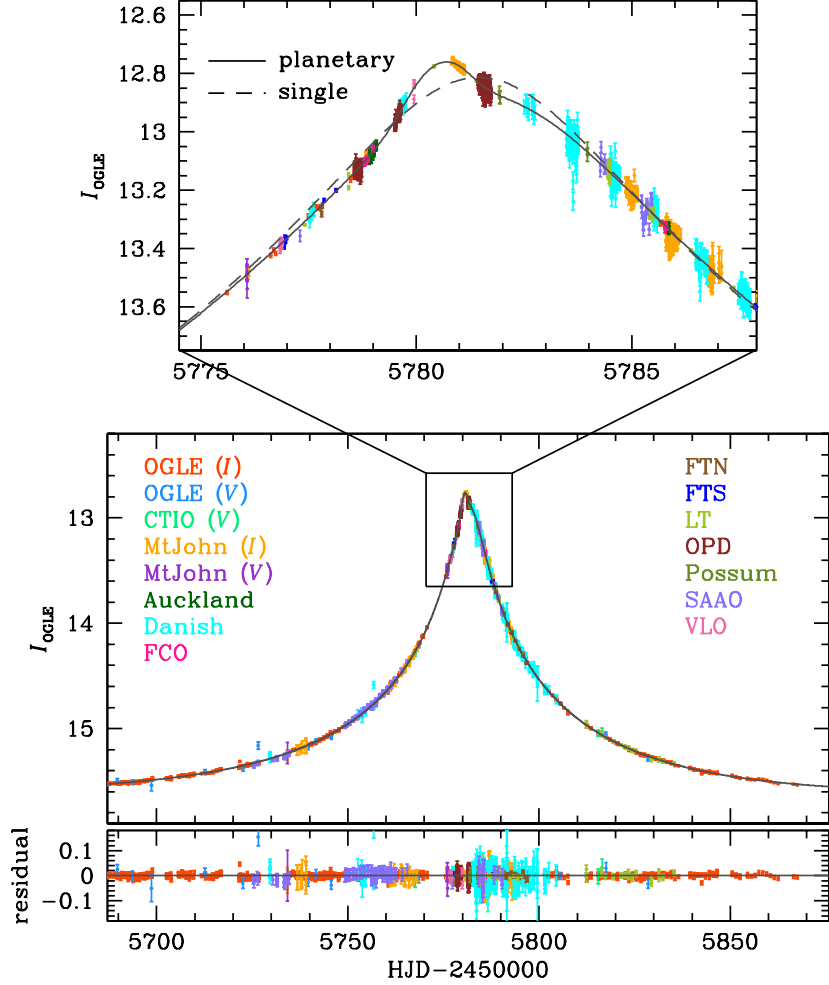


Figure 1. Light curve of OGLE-2011-BLG-0251. Data points are plotted with $1\text{-}\sigma$ error bars, and the upper panel shows a zoom around the perturbation region near the peak

In Fig. 2, we show χ^2 of the fit plotted as a function of the orbital period of the source star. We compare this to the χ^2 statistic of the best parallax fit. We find that xallarap models provide fits competitive with the parallax planetary models for orbital periods $P > 1$ year. However, the solutions in this range cannot meet the constraint provided by the source brightness. Combining Equations (6) and (7) with Kepler’s third law, $P^2 = a^3/(M_1 + M_2)$ yields (Dong et al. 2009)

$$P^2 = \frac{(M_1 + M_2)^2}{M_2^3} \left(\frac{\xi_E \hat{r}_E}{\text{AU}} \right)^3. \quad (8)$$

Rearranging this equation for M_2 , and using the fact that $M_2/(M_1 + M_2) < 1$, we can derive an upper limit for the mass of M_2 ,

$$M_{2,\text{min}} = \frac{(\xi_E \hat{r}_E)^3}{P^2}. \quad (9)$$

In the lower panel of Fig. 2, we show the minimum mass of the source companion as a function of orbital period. The blending constraint means that the source companion cannot be arbitrarily massive, and we use a conservative

upper limit for its mass of $3 M_\odot$. With this constraint, we find that xallarap models are not competitive with parallax planetary models, and we therefore exclude the xallarap interpretation of the light curve.

4.1.2. Binary source

We also attempted to model this event as a binary source - point lens (BSPL) event. For this we introduced three additional parameters: the impact parameter of the secondary source component, $u_{0,2}$, and its time of closest approach, $t_{0,2}$, as well the flux ratio between the source components. We note that parallax is also considered in our binary source modelling, for fair comparison to other models. We find that the best binary-source model provides a poorer fit, with $\chi^2 = 3809$, which gives $\Delta\chi^2 \sim 180$ compared to our best planetary model (including parallax, see model D in the following section). Residuals for this model, as well as all other models discussed in this section are shown in Fig. 3.

Team and telescope	filter	Aperture	Location	N	a	b
OGLE	I	1.3m	Las Campanas, Chile	1527	0.369	0.020
OGLE	V	1.3m	Las Campanas, Chile	27	0.937	0.010
MiNDSTEp Danish	I	1.54m	La Silla, Chile	454	1.085	0.020
LCOGT Liverpool Telescope	I	2m	La Palma, Canary Islands	191	2.434	0.001
LCOGT Faulkes North	I	2m	Haleakala, Hawai'i	41	1.806	0.005
LCOGT Faulkes South	I	2m	Siding Spring Observatory, Australia	31	1.119	0.005
μ FUN CTIO	V	1.3m	Cerro Tololo, Chile	6	1.000	0.020
μ FUN Auckland	R	0.4m	Auckland, New Zealand	60	1.027	0.010
μ FUN Farm Cove	–	0.36m	Auckland, New Zealand	47	0.841	0.005
μ FUN Possum	R	0.36m	Gisborne, New Zealand	5	1.000	0.020
μ FUN Vintage Lane	–	0.4m	Blenheim, New Zealand	17	2.055	0.001
μ FUN Pico dos Dias	I	0.6m	Minas Gerais, Brazil	572	3.095	0.001
MOA Mt John B&C	I	0.6m	South Island, New Zealand	621	5.175	0.001
MOA Mt John B&C	V	0.6m	South Island, New Zealand	5	1.000	0.020
PLANET SAAO	I	1m	SAAO, South Africa	134	1.931	0.010
Total				3738		

Table 1. Data sets for OGLE-2011-BLG-0251, with the number of data points for each telescope/ filter combination. The rescaling coefficients a and b are also given, with error bars rescaled as $\sigma' = a\sqrt{\sigma^2 + b^2}$, where σ' is the rescaled error bar and σ is the original error bar.

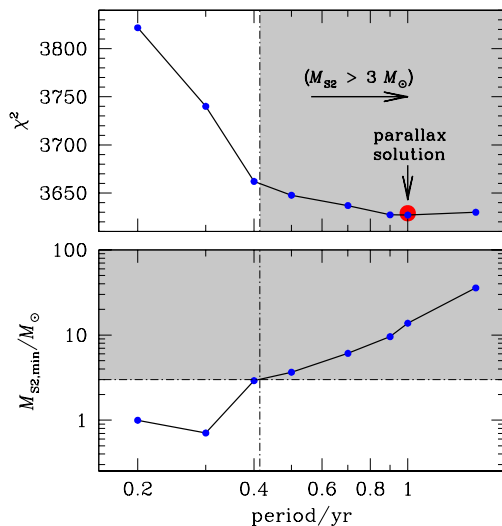


Figure 2. Constraints from the xallarap fit as a function of the orbital period P of the source star. The top panel shows χ^2 of the xallarap fit as a function of P , with a red circle marking the location of the best parallax model. The bottom panel shows the minimum mass of the source companion as a function of P . The shaded area in both panels indicates where models are excluded based on conservative blending constraints on the source companion’s mass.

4.2. Best-fit models

We searched the parameter space using an MCMC algorithm as well as a grid of (d, q, α) to locate good starting points for the algorithm (see e.g. Kains et al. 2009), over the range $-4 < \log q < 0$ and $-1.0 < \log d < 2$. This encompasses both planetary and binary companions that might cause the central perturbation. In Fig. 4 we present the χ^2 distribution in the d, q plane. We find four local solutions, all of which have a mass ratio corresponding to a planetary companion. We designate them as A, B, C and D;

the degeneracy among these local solutions is rather severe, as can be seen from the residuals shown in Fig. 3.

For the identified local minima, we then further refine the lensing parameters by conducting additional modelling, considering higher-order effects of the finite source size and the Earth’s orbital motion. It is found that the higher-order effects are clearly detected with $\Delta\chi^2 > 500$. Best-fit parameter for each of the local minima are given in Table 2, while Fig. 5 shows the geometry of the source trajectories with respect to the caustics for all four minima. We note that the pairs of solutions A and D, and B and C, are degenerate under the well-known $d \leftrightarrow d^{-1}$ degeneracy (Griest & Safizadeh 1998; Dominik 1999); this is caused by the symmetry of the lens mapping between binaries with d and d^{-1} . Comparing the pairs of solutions, we find that the A-D pair is favoured, with $\Delta\chi^2 > 40$ compared to the B-C pair. On the other hand, the degeneracy between the A and D solutions is very severe, with only $\Delta\chi^2 \sim 7$. In Fig. 6, we also show parameter-parameter correlations plots for model D, showing also the uncertainties in the measured lensing parameters.

5. Lens Properties

In this section we determine the properties of the lens system, using our best-fit model parameters, i.e. our wide-configuration ESBL + parallax model. We also calculated the lens properties for the competitive close-configuration model, with both sets of parameter values listed in Table 3.

5.1. Source star and Einstein radius

We determined the Einstein radius by first calculating the angular size of the source. This can be done by using the magnitude and colour of the source (e.g. Yoo et al. 2004), and empirical relations between these quantities and the angular source size. We start by using the location of the red giant clump (hereafter RC) on our colour-magnitude diagram (Fig. 7) to estimate the reddening and extinction along the line of sight. We use an I -band absolute magnitude for the RC of $M_{I,RC,0} = -0.12 \pm 0.09$ (Nataf et al. 2012), as well as a colour $(V - I)_{RC,0} = 1.06 \pm 0.12$

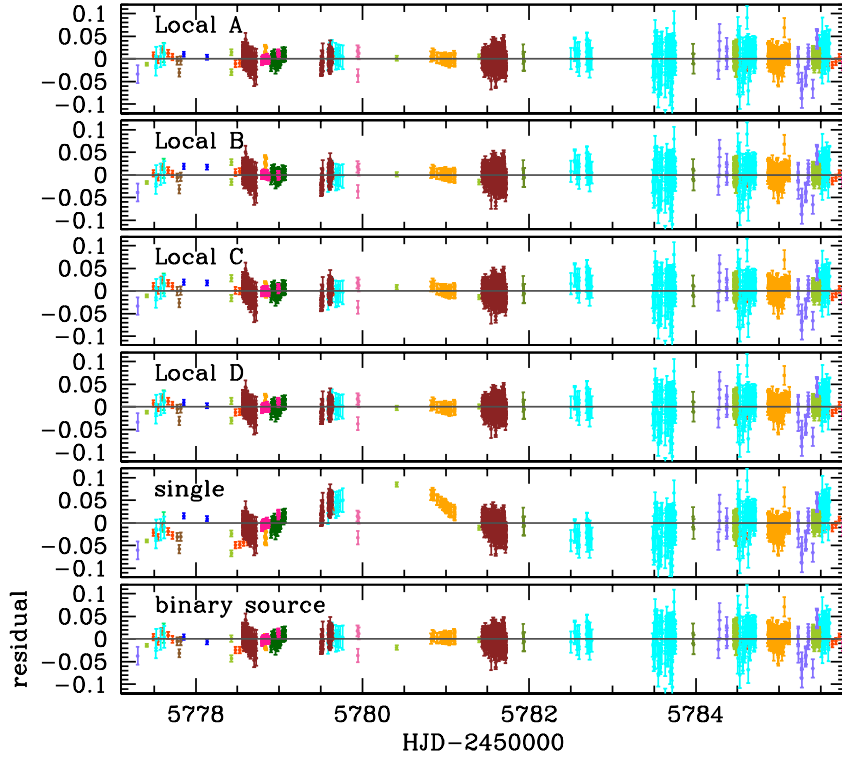


Figure 3. Residual of data, with $1\text{-}\sigma$ error bars, for the various models considered.

Parameter	Local A	Local B	Local C	Local D
χ^2	3636	3698	3675	3629
<i>d.o.f.</i>	3699	3699	3699	3699
t_0 [MHJD]	5781.509 ± 0.004	5781.472 ± 0.004	5781.487 ± 0.004	5781.503 ± 0.004
t_E [days]	63.74 ± 0.41	64.05 ± 0.46	64.24 ± 0.47	63.88 ± 0.46
α [rad]	-1.855 ± 0.002	-1.845 ± 0.002	-1.849 ± 0.004	-1.855 ± 0.002
$u_0/10^{-2}$	-5.66 ± 0.04	-5.63 ± 0.04	-5.64 ± 0.05	-5.63 ± 0.04
$\rho_*/10^{-2}$	1.44 ± 0.05	1.77 ± 0.04	1.87 ± 0.08	1.39 ± 0.05
d	0.775 ± 0.010	0.997 ± 0.009	1.066 ± 0.001	1.408 ± 0.019
$q/10^{-3}$	(1.68 ± 0.11)	(0.93 ± 0.03)	(1.11 ± 0.06)	(1.92 ± 0.12)
$\pi_{E,N}$	-0.33 ± 0.04	-0.37 ± 0.04	-0.40 ± 0.05	-0.34 ± 0.05
$\pi_{E,E}$	0.09 ± 0.01	0.08 ± 0.01	0.08 ± 0.01	0.09 ± 0.01
π_E	0.34 ± 0.04	0.38 ± 0.04	0.41 ± 0.05	0.35 ± 0.05
${}^a g = F_B/F_S$	0.387 ± 0.035	0.394 ± 0.001	0.394 ± 0.042	0.376 ± 0.017
${}^a I_S$	15.99 ± 0.03	15.98 ± 0.01	15.98 ± 0.02	15.97 ± 0.01
${}^a I_B$	16.97 ± 0.07	16.99 ± 0.01	16.99 ± 0.06	17.04 ± 0.03

Table 2. Best-fit model parameters and $1\text{-}\sigma$ error bars for the four identified best binary-lens models including the effects of the orbital motion of the Earth (parallax). MHJD \equiv HJD-2450000. ^afor the OGLE data set

(Bensby et al. 2011). We compare these values to those on our colour-magnitude diagram (CMD), which we generated using OGLE I - and V - band photometry. From Fig. 7, the location of the RC on our CMD is

$$(I, V - I)_{\text{RC}} = (17.19 \pm 0.05, 3.45 \pm 0.05) \quad (10)$$

so, using a distance modulus of $\mu = 14.52 \pm 0.09$, i.e. a distance to the Galactic bulge of 8.0 ± 0.3 kpc (Yelda et al. 2011), we find $A_I = 2.79 \pm 0.10$ and $E(V - I) = 2.39 \pm 0.13$.

Using these values, the best-fit value for the magnitude of the source $I_S = 15.97 \pm 0.01$, a source colour $(V - I)_{S,0} = 1.15$, and the empirical relations of Kervella & Fouqué (2008), we find an angular source radius $\theta_* = 10.41 \pm$

$1.18 \mu\text{s}$, or a source star radius of $R_* = 10.53 \pm 1.19 R_\odot$. This, together with the best-fit value of the source size parameter ρ_* , allows us to calculate the size of the Einstein radius, $\theta_E = \theta_*/\rho_*$. Using the relevant parameter values, we find $\theta_E = 0.749 \pm 0.283$ mas. This in turn allows us to calculate the source-lens relative proper motion, $\mu_{\text{rel}} = \theta_E/t_E = 4.28 \pm 1.62$ mas/yr.

5.2. Masses of the Lens Components

Combining Eq. (1) and Eq. (5) allows us to derive an expression for the mass as a function of the parallax vector magnitude π_E (defined by Eq. 4):

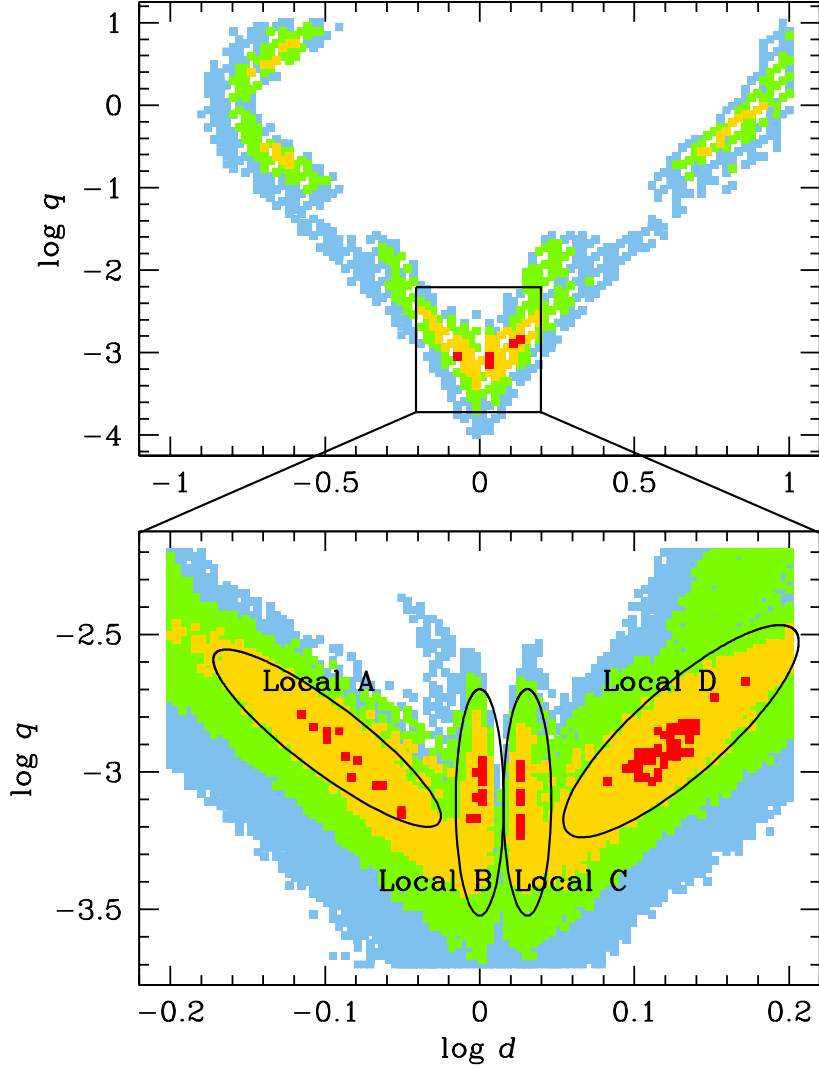


Figure 4. χ^2 map in the d, q plane, showing the location of the four local minima identified by our modelling runs. Out of these, local minima *A* and *D* are competitive, with local minima *B* and *C* having $\Delta\chi^2 \sim 50$ and 70 respectively, for the same number of parameters. Minima *A* and *D* correspond to the close and wide ESBL + parallax models discussed in the text. Different colours correspond to $\Delta\chi^2 < 25$ (red), 100 (yellow), 225 (green), and 400 (blue); we note that the χ^2 map is based on the original data, before error-bar normalisation, and therefore the $\Delta\chi^2$ levels are slightly different from those given in Table 2. The top panel shows the breadth of our parameter space exploration, encompassing planetary and non-planetary mass-ratio regimes, while the bottom panel shows a zoom on the region where our local minima are located.

$$M_L = \frac{\theta_E c^2}{4G\pi_E} \quad (11)$$

Using values found in the previous section, and our best-fit parallax parameter value $\pi_E = 0.35 \pm 0.05$ yields a total lens mass $M_L = 0.26 \pm 0.10 M_\odot$. Using the best-fit mass ratio parameter value of $q = (1.92 \pm 0.12) \times 10^{-3}$ yields component masses of $0.26 \pm 0.11 M_\odot$ and $0.53 \pm 0.21 M_J$, where M_J is the mass of Jupiter.

5.3. Distance to the Lens

We can also rearrange Eq. (1) to derive an expression for the distance to the lens D_L ,

$$D_L = \left[\frac{1}{D_S} + \frac{\theta_E^2 c^2}{4GM} \right]^{-1}. \quad (12)$$

Using our parameter values as well as the lens mass derived thanks to our parallax measurement, we find a distance to the lens of $D_L = 2.57 \pm 0.61$ kpc. This distance allows us to carry out a sanity check of the lens mass we derived in the previous section. By assuming that the contribution from the blended light comes from the lens, we can derive an upper limit to the I -band lens magnitude M_I using our best-fit blending parameter:

$$M_{I,L} = m_{I,b} - 5 \log_{10} D_L - 10 - A_{I,L}, \quad (13)$$

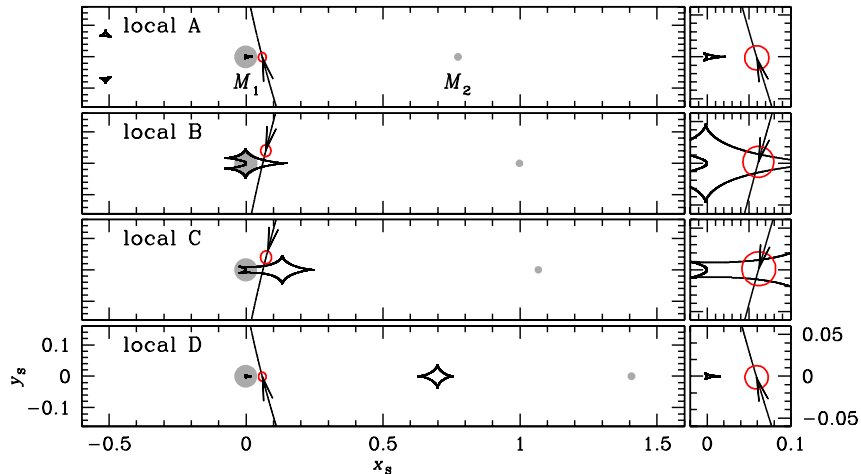


Figure 5. Source trajectory geometry with respect to the caustics for all four local minima identified in Fig. 4; the source size is marked as a red circle.

where $m_{I,b}$ is the apparent I -band magnitude of the blend, $A_{I,L}$ is the extinction between the observer and the lens, and D_L is in kpc. In practice, $A_{I,L} \leq A_I$ since the lens is in front of the source, so we use the extreme scenario where $A_{I,L} = A_I$ to derive an upper brightness limit (lower limit on the magnitude) for the lens. We find this to be $M_{I,L} = 2.19 \pm 0.53$ mag, which corresponds to a maximum mass of the lens of $M_{L,\max} = 1.65 \pm 0.23 M_\odot$, assuming a main sequence star mass-luminosity relation, and assuming that the secondary lens component (i.e. the planet) does not contribute to the blended light. This is much larger than the value we derived in Sec. 5.2 for the mass of the primary lens component, which suggests that some blending comes from stars near the source rather than from the lens, although it is difficult to quantify this without an estimate of $A_{I,L}$.

Finally, we can also use the distance to the lens and the size of the Einstein ring radius to calculate the projected separation r_\perp between the lens components in AU. Using our best-fit projected angular separation $d = 1.408 \pm 0.019$, we find a projected (i.e. minimum) orbital radius $r_\perp = 2.72 \pm 0.75$ AU.

We can compare this to an estimate of the location of the “snow line”, which is the location at which water sublimated in the midplane of the protoplanetary disk, i.e. the distance at which the midplane had a temperature of $T_{\text{mid}} = 170$ K (although other studies have noted that this temperature varies; see e.g. Podolak & Zucker 2004). The core accretion model of planet formation predicts that giant planets form much more easily beyond the snow line, thanks to easier condensation of icy material and therefore easier formation of large solid cores in the early stages of the circumstellar disk’s evolution. Kennedy & Kenyon (2008) modelled the evolution of the snow line’s location, taking into account heating of the disk via accretion, as well as the influence of pre-main sequence stellar evolution. Using a rough extrapolation of their results, we estimate that the snow line (at $t = 1$ Myr) for the planetary host star in OGLE-2011-BLG-0251 is located at around ~ 1 – 1.5 AU. We therefore conclude that OGLE-2011-BLG-0251Lb is a giant planet located beyond the snow line, with both of our competitive best-fit models yielding projected orbital radii larger than 1.5 AU.

	close	wide
θ_* [μas]	10.29 ± 1.17	10.41 ± 1.18
θ_E [mas]	0.71 ± 0.26	0.75 ± 0.28
μ_{rel} [mas yr^{-1}]	4.09 ± 1.50	4.28 ± 1.62
M_1 [M_\odot]	0.26 ± 0.10	0.26 ± 0.11
M_2 [M_J]	0.45 ± 0.18	0.53 ± 0.21
$M_{L,\max}$	1.71 ± 0.23	1.65 ± 0.23
D_L [kpc]	2.71 ± 0.61	2.57 ± 0.61
r_\perp [AU]	1.50 ± 0.50	2.72 ± 0.75

Table 3. Lens properties derived as detailed in Sec. 5, for both competitive parallax models.

We list all the lens properties in Table 3, both for the best-fit model parameters that we have used above, and for the close-configuration model, for comparison. Lens properties derived using the close-configuration model are very similar to those we found using the wide-configuration model, the only major difference being in the orbital radius. For the close model, we find an orbital radius of 1.50 ± 0.50 AU, which is close to the location of the snow line.

6. Conclusions

Our coverage and analysis of OGLE-2011-BLG-0251 has allowed us to locate and constrain a best-fit binary-lens model corresponding to an M star being orbited by a giant planet. This was possible through a broad exploration of the parameters both in real time, thanks to the recent developments in microlensing modelling algorithms, and after the source had returned to its baseline magnitude. Various second-order effects, as well as other possible, non-planetary, interpretations for the anomaly were considered during the modelling process. Based on the best-fit solution, we were able to constrain the masses and separation of the lens components, as well as various other characteristics, thanks to a strong detection of parallax effects due to the Earth’s orbit around the Sun, in conjunction with the detection of finite source size effects. We found a planet of mass $0.53 \pm 0.21 M_J$ orbiting a lens of $0.26 \pm 0.11 M_\odot$ at a projected radius $r_\perp = 2.72 \pm 0.75$ AU; the whole

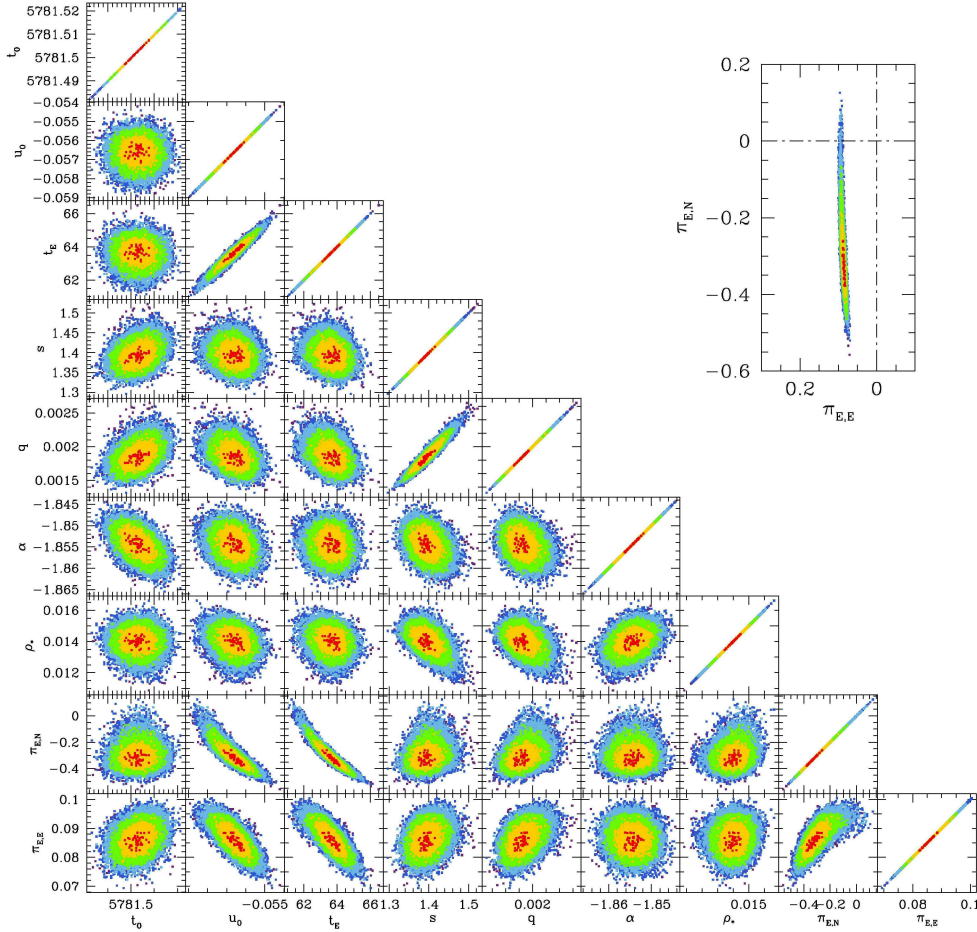


Figure 6. Parameter-parameter correlations for our 9 fitted parameters. Colours indicate the limits of the 1, 2, 3, 4 and 5- σ confidence limits for each pairwise distribution. A closer view of the correlation between parallax parameters is shown on the top right inset.

system is located at a distance of 2.57 ± 0.61 kpc. Our competitive second-best model leads to similar properties, but a smaller projected orbital radius $r_{\perp} = 1.50 \pm 0.50$. The two best-fit models are competitive and therefore we cannot make a strong claim about which orbital radius is favoured. However, comparing both values of the projected orbital radius to the approximate location of the snow line for a typical star of the mass of the primary lens component, we conclude that OGLE-2011-BLG-0251Lb is a giant planet located around or beyond the snow line. This is in line with predictions from the core accretion model of planet formation, from which we expect large planets to be more numerous beyond the snow line; this is also where microlensing detection sensitivity is at its highest, enabling us to probe a region of planetary parameter space that is difficult to reach for other methods.

Acknowledgements

NK acknowledges an ESO Fellowship. The research leading to these results has received funding from the European Community’s Seventh Framework Programme (/FP7/2007-2013/) under grant agreements No 229517 and 268421. The OGLE project has received funding from the European Research Council under the European Community’s Seventh Framework Programme

(FP7/2007-2013) / ERC grant agreement no. 246678 to AU. KA,DB,MD,KH,MH,SI,CL,RS,YT are supported by NPRP grant NPRP-09-476-1-78 from the Qatar National Research Fund (a member of Qatar Foundation). Work by C. Han was supported by Creative Research Initiative Program (2009-0081561) of National Research Foundation of Korea. This work is based in part on data collected by MiNDSTEP with the Danish 1.54m telescope at the ESO La Silla Observatory. The Danish 1.54m telescope is operated based on a grant from the Danish Natural Science Foundation (FNU). The MiNDSTEP monitoring campaign is powered by ARTEMiS (Automated Terrestrial Exoplanet Microlensing Search; Dominik et al. 2008). MH acknowledges support by the German Research Foundation (DFG). DR (boursier FRIA), OW (aspirant FRS - FNRS) and J. Surdej acknowledge support from the Communauté française de Belgique – Actions de recherche concertées – Académie universitaire Wallonie-Europe. TCH gratefully acknowledges financial support from the Korea Research Council for Fundamental Science and Technology (KRCF) through the Young Research Scientist Fellowship Program. TCH and CUL acknowledges financial support from KASI (Korea Astronomy and Space Science Institute) grant number 2012-1-410-02. Work by J.C. Yee is supported by a National Science Foundation Graduate Research Fellowship under Grant No. 2009068160. A. Gould and B.S. Gaudi ac-

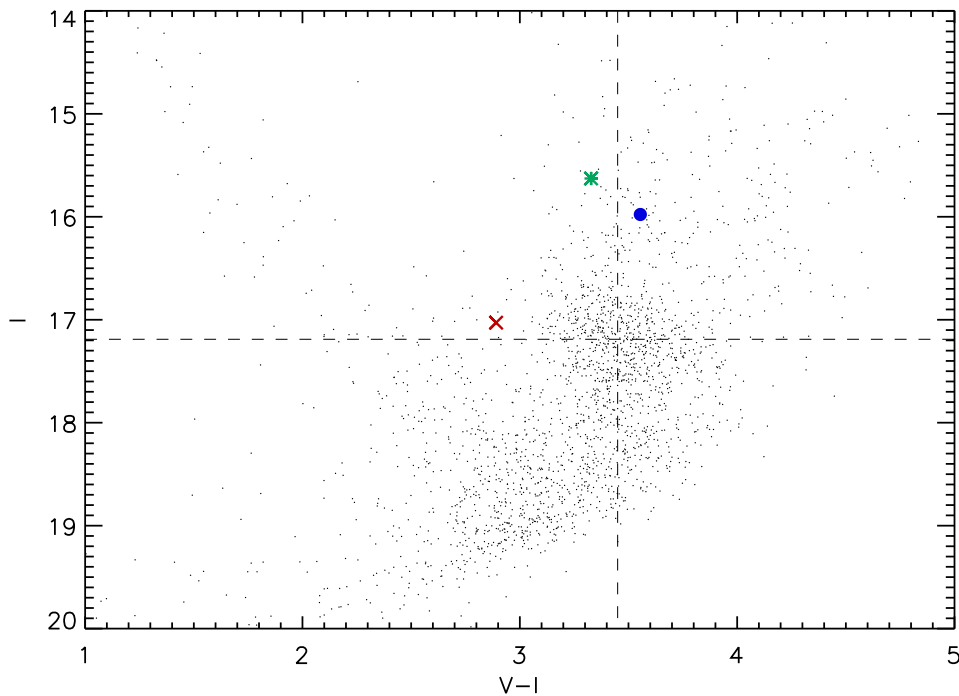


Figure 7. $V - I, I$ colour-magnitude diagram of the OGLE-2011-BLG-0251 field obtained using OGLE-IV photometry. The location of the total source + blend is indicated by a green asterisk, while the location of the deblended source is marked by a blue filled circle, and that of the blend by a red cross. The dashed lines cross at the location of the Red Clump.

knowledge support from NSF AST-1103471. B.S. Gaudi, A. Gould, and R.W. Pogge acknowledge support from NASA grant NNX12AB99G. The MOA experiment was supported by grants JSPS22403003 and JSPS23340064. TS was supported by the grant JSPS23340044. Y. Muraki acknowledges support from JSPS grants JSPS23540339 and JSPS19340058.

References

- An, J. H., Albrow, M. D., Beaulieu, J.-P., et al. 2002, *ApJ*, 572, 521
 Beaulieu, J.-P. et al. 2006, *Nature*, 439, 437
 Bennett, D. P. 2010, *ApJ*, 716, 1408
 Bensby, T., Adén, D., Meléndez, J., et al. 2011, *A&A*, 533, A134
 Bozza, V., Dominik, M., Rattenbury, N. J., et al. 2012, *MNRAS*, 424, 902
 Bramich, D. M. 2008, *MNRAS*, 386, L77
 Bramich, D. M., Horne, K., Albrow, M. D., et al. 2013, *MNRAS*, 428, 2275
 Cassan, A. 2008, *A&A*, 491, 587
 Cassan, A., Kubas, D., Beaulieu, J.-P., et al. 2012, *Nature*, 481, 167
 Claret, A. 2000, *A&A*, 363, 1081
 Dominik, M. 1998, *A&A*, 329, 361
 Dominik, M. 1999, *A&A*, 341, 943
 Dominik, M., Horne, K., Allan, A., et al. 2008, *Astronomische Nachrichten*, 329, 248
 Dong, S., Gould, A., Udalski, A., et al. 2009, *ApJ*, 695, 970
 Einstein, A. 1936, *Science*, 84, 506
 Gaudi, B. S. et al. 2008, *Science*, 319, 927
 Gould, A. 2004, *ApJ*, 606, 319
 Gould, A., Dong, S., Gaudi, B. S., et al. 2010, *ApJ*, 720, 1073
 Griest, K. & Hu, W. 1992, *ApJ*, 397, 362
 Griest, K. & Safizadeh, N. 1998, *ApJ*, 500, 37
 Kains, N., Browne, P., Horne, K., Hundertmark, M., & Cassan, A. 2012, *MNRAS*, 426, 2228
 Kains, N., Cassan, A., Horne, K., et al. 2009, *MNRAS*, 395, 787
 Kennedy, G. M. & Kenyon, S. J. 2008, *ApJ*, 673, 502
 Kervella, P. & Fouqué, P. 2008, *A&A*, 491, 855
 Lupton, R. 1993, *Statistics in theory and practice*
 Muraki, Y., Han, C., Bennett, D. P., et al. 2011, *ApJ*, 741, 22
 Nataf, D. M., Gould, A., Fouqué, P., et al. 2012, *ArXiv e-prints*
 Podolak, M. & Zucker, S. 2004, *Meteoritics and Planetary Science*, 39, 1859
 Ryu, Y.-H., Han, C., Hwang, K.-H., et al. 2010, *ApJ*, 723, 81
 Sumi, T., Kamiya, K., Bennett, D. P., et al. 2011, *Nature*, 473, 349
 Udalski, A. 2003, *Acta Astronomica*, 53, 291
 Yelda, S., Ghez, A. M., Lu, J. R., et al. 2011, in *Astronomical Society of the Pacific Conference Series*, Vol. 439, *The Galactic Center: a Window to the Nuclear Environment of Disk Galaxies*, ed. M. R. Morris, Q. D. Wang, & F. Yuan, 167
 Yoo, J., DePoy, D. L., Gal-Yam, A., et al. 2004, *ApJ*, 603, 139

¹ European Southern Observatory, Karl-Schwarzschild Straße 2, 85748 Garching bei München, Germany

² Las Cumbres Observatory Global Telescope Network, 6740 Cortona Drive, Suite 102, Goleta, CA 93117, USA

³ Department of Physics, Institute for Astrophysics, Chungbuk National University, Cheongju 371-763, Korea

⁴ Warsaw University Observatory, Al. Ujazdowskie 4, 00-478 Warszawa, Poland

⁵ Divisão de Astrofísica, Instituto Nacional de Pesquisas Especiais, Avenida dos Astronautas, 1758 Sao José dos

- Campos, 12227-010 SP, Brazil
- ⁶ School of Chemical and Physical Sciences, Victoria University, Wellington, New Zealand
- ⁷ Niels Bohr Institute, University of Copenhagen, Juliane Maries vej 30, 2100 Copenhagen, Denmark
- ⁸ Centre for Star and Planet Formation, Geological Museum, Øster Voldgade 5, 1350 Copenhagen, Denmark
- ⁹ Qatar Foundation, P.O. Box 5825, Doha, Qatar
- ¹⁰ Dipartimento di Fisica “E.R. Caianiello”, Università di Salerno, Via Ponte Don Melillo, 84084 Fisciano, Italy
- ¹¹ Istituto Nazionale di Fisica Nucleare, Sezione di Napoli, Italy
- ¹² SUPA School of Physics & Astronomy, University of St Andrews, North Haugh, St Andrews, KY16 9SS, United Kingdom
- ¹³ Deutsches SOFIA Institut, Universität Stuttgart, Pfaffenwaldring 31, 70569 Stuttgart, Germany
- ¹⁴ SOFIA Science Center, NASA Ames Research Center, Mail Stop N211-3, Moffett Field CA 94035, United States of America
- ¹⁵ Istituto Internazionale per gli Alti Studi Scientifici (IIASS), Vietri Sul Mare (SA), Italy
- ¹⁶ Institut für Astrophysik, Georg-August-Universität, Friedrich-Hund-Platz 1, 37077 Göttingen, Germany
- ¹⁷ Korea Astronomy and Space Science Institute, Daejeon 305-348, Korea
- ¹⁸ National Astronomical Observatories/Yunnan Observatory, Joint laboratory for Optical Astronomy, Chinese Academy of Sciences, Kunming 650011, People’s Republic of China
- ¹⁹ Department of Physics and Astronomy, Aarhus University, Ny Munkegade 120, 8000 Århus C, Denmark
- ²⁰ Armagh Observatory, College Hill, Armagh, BT61 9DG, Northern Ireland, United Kingdom
- ²¹ Danmarks Tekniske Universitet, Institut for Rumforskning og -teknologi, Juliane Maries Vej 30, 2100 København, Denmark
- ²² Jodrell Bank Centre for Astrophysics, University of Manchester, Oxford Road, Manchester, M13 9PL, UK
- ²³ Max Planck Institute for Astronomy, Königstuhl 17, 69117 Heidelberg, Germany
- ²⁴ Department of Astronomy, Ohio State University, 140 West 18th Avenue, Columbus, OH 43210, United States of America
- ²⁵ Department of Physics, Sharif University of Technology, P. O. Box 11155–9161, Tehran, Iran
- ²⁶ Perimeter Institute for Theoretical Physics, 31 Caroline St. N., Waterloo ON, N2L 2Y5, Canada
- ²⁷ Institut d’Astrophysique et de Géophysique, Allée du 6 Août 17, Sart Tilman, Bât. B5c, 4000 Liège, Belgium
- ²⁸ Space Telescope Science Institute, 3700 San Martin Drive, Baltimore, MD 21218, United States of America
- ²⁹ INFN, Gruppo Collegato di Salerno, Sezione di Napoli, Italy
- ³⁰ European Southern Observatory (ESO), Alonso de Cordova 3107, Casilla 19001, Santiago 19, Chile
- ³¹ Max Planck Institute for Solar System Research, Max-Planck-Str. 2, 37191 Katlenburg-Lindau, Germany
- ³² Astrophysics Group, Keele University, Staffordshire, ST5 5BG, United Kingdom
- ³³ Astronomisches Rechen-Institut, Zentrum für Astronomie der Universität Heidelberg (ZAH), Mönchhofstr. 12-14, 69120 Heidelberg, Germany
- ³⁴ Institute of Astronomy, University of Cambridge, Madingley Road, Cambridge CB3 0HA, United Kingdom
- ³⁵ Alsubais Establishment for Scientific Studies, Doha, Qatar
- ³⁶ Astrophysics Research Institute, Liverpool John Moores University, Twelve Quays House, Egerton Wharf,

- Birkenhead, Wirral., CH41 1LD, UK
- 37 School of Mathematical Sciences, Queen Mary, University of London, Mile End Road, London E1 4NS, UK
- 38 Vintage Lane Observatory, Blenheim, New Zealand
- 39 Auckland Observatory, Auckland, New Zealand
- 40 Dept. of Physics and Astronomy, Texas A&M University College Station, TX 77843-4242, USA
- 41 Possum Observatory, Patutahi, Gisbourne, New Zealand
- 42 Farm Cove Observatory, Centre for Backyard Astrophysics, Pakuranga, Auckland, New Zealand
- 43 Institute for Radiophysics and Space Research, AUT University, Auckland, New Zealand
- 44 Dept. of Astronomy and Space Science, Chungnam University, Korea
- 45 Departamento de Astronomía y Astrofísica, Universidad de Valencia, E-46100 Burjassot, Valencia, Spain
- 46 UPMC-CNRS, UMR7095, Institut d'Astrophysique de Paris, 98bis boulevard Arago, F-75014, Paris, France
- 47 University of Canterbury, Dept. of Physics and Astronomy, Private Bag 4800, Christchurch 8020, New Zealand
- 48 McDonald Observatory, 16120 St Hwy Spur 78 #2, Fort Davis, Tx 79734, USA
- 49 University of the Free State, Faculty of Natural and Agricultural Sciences, Dept. of Physics, P.O. Box 339, Bloemfontein 9300, South Africa
- 50 School of Math and Physics, University of Tasmania, Private Bag 37, GPO Hobart, Tasmania 7001, Australia
- 51 Institute of Geophysics and Planetary Physics (IGPP), L-413, Lawrence Livermore National Laboratory, P.O. Box 808, Livermore, CA 94551, USA
- 52 Universit de Toulouse; UPS-OMP; IRAP; Toulouse, France
- 53 CNRS; IRAP; 14, avenue Edouard Belin, F-31400 Toulouse, France
- 54 Physics Department, Faculty of Arts and Sciences, University of Rijeka, Omladinska 14, 51000 Rijeka, Croatia
- 55 Technical University of Vienna, Department of Computing, Wiedner Hauptstrasse 10, Vienna, Austria
- 56 NASA Exoplanet Science Institute, Caltech, MS 100-22, 770 S. Wilson Ave., Pasadena, CA 91125, USA
- 57 Perth Observatory, Walnut Road, Bickley, Perth 6076, Australia
- 58 South African Astronomical Observatory, P.O. Box 9, Observatory 7935, South Africa
- 59 Solar-Terrestrial Environment Laboratory, Nagoya University, Nagoya, 464-8601, Japan
- 60 Dept. of Physics, University of Notre Dame, Notre Dame, IN 46556, USA
- 61 Institute of Information and Mathematical Sciences, Massey University, Private Bag 102-904, North Shore Mail Centre, Auckland, New Zealand
- 62 Dept. of Physics, University of Auckland, Private Bag 92019, Auckland, New Zealand
- 63 Okayama Astrophysical Observatory, National Astronomical Observatory of Japan, Asakuchi, Okayama 719-0232, Japan
- 64 Mt. John Observatory, P.O. Box 56, Lake Tekapo 8770, New Zealand
- 65 Dept. of Physics, Konan University, Nishiokamoto 8-9-1, Kobe 658-8501, Japan
- 66 Nagano National College of Technology, Nagano, 381-8550, Japan
- 67 Tokyo Metropolitan College of Industrial Technology, Tokyo, 116-8523, Japan
- 68 Dept. of Earth and Space Science, Graduate School of Science, Osaka University, 1-1 Machikaneyama-cho, Toyonaka, Osaka 560-0043, Japan
- 69 Universidad de Concepción, Departamento de Astronomía, Casilla 160-C, Concepción, Chile